Oxygen vacancy order-disorder transition at high temperature in Bi-Sr-Fe-based perovskite-type oxides

Yuto Tomura, Itaru Oikawa, and Hitoshi Takamura *

Department of Materials Science, Graduate School of Engineering, Tohoku University, Sendai 980-8579, Japan

(Received 16 May 2019; revised manuscript received 30 September 2019; published 2 December 2019)

$Bi_{1-x}Sr_xFeO_{3-\delta}$ (BSFs) are well known not only as multiferroic materials but also as mixed oxide-ion and electronic conductors. BSFs show remarkable ionic conductivity despite their limited electrochemical activity due to their low electronic conductivity. In this study, the discontinuous change in the electrical conductivity of $Bi_{0.7}Sr_{0.3}FeO_{3-\delta}$ (BSF30) at around 770 °C was investigated in the context of their unique defect order-disorder transition. Based on the electrical conductivity and the Seebeck coefficient of BSF30, both functions of temperature and oxygen partial pressure, the discontinuous change in both hole and oxide-ion conductivities was the result of a reduction in their mobility but unrelated to their concentration term. High-temperature x-ray diffraction and scanning transmission electron microscopy revealed that periodic oxygen-deficient planes with fivefold d-spacing of {001} emerge in an ordered low-temperature phase while the ordered defect structure disappears in a high-temperature phase. The discontinuous change of electrical conductivity of BSF30 was then found to be the result of the order-disorder transition of its oxygen sublattice, i.e., oxygen vacancies. Because there was no such transition in the cation sublattice, the cation did not affect the electrical conductivity of BSF30. This study suggests that BSFs with the desired electrochemical and multiferroic functionalities can be designed by controlling their order-disorder transition.

DOI: 10.1103/PhysRevMaterials.3.125802

I. INTRODUCTION

$BiFeO_3$ (BFO) with a perovskite-type structure is well known as a multiferroic material that shows both antiferromagnetic and ferroelectric properties simultaneously. Because of this remarkable trait, there is considerable interest in its potential for use in memory devices [1]. Its application is, however, limited because of its weak magnetoelectric coupling. Therefore, in an attempt to improve its magnetic property, various elemental substitutions have been investigated. It has been shown, for example, that ferromagnetism emerges by substituting Sr for the Bi-site [2].

Since Brinkman *et al.* reported that $Bi_{1-x}Sr_xFeO_{3-\delta}$ (BSFs) are not only multiferroic materials but also mixed oxide-ion and electronic conductors (MIECs) [3], BSFs have been considered promising materials for use in electrochemical devices operated at high temperature, such as solid oxide fuel cells (SOFCs) and oxygen permeation membranes (OPMs). Niu *et al.* have reported that $Bi_{0.5}Sr_{0.5}FeO_{3-\delta}$ shows remarkable SOFC cathode properties, including a low area specific resistance (ASR) of 0.12 $\Omega\,cm^2$ and a low cathode overpotential of 10.2 mV as a Co-free material [4]. Its cathode performance can be further improved by Co-substitution: Khaerudini *et al.* reported remarkably low polarization resistances of $Bi_{0.3}Sr_{0.7}Co_{0.3}Fe_{0.7}O_{3-\delta}$ and $(Bi_{0.4}Sr_{0.6})_{0.8}Co_{0.3}Fe_{0.7}O_{3-\delta}$ at 0.076 and 0.10 $\Omega\,cm^2$, respectively [5,6]. In their investigation of the potential of $Bi_{0.2}Sr_{0.8}FeO_{3-\delta}$ as an oxygen permeation membrane, Brinkman *et al.* reported a high oxygen flux density of 0.11 μmol cm^{-2} s^{-1} at 800 °C [7].

These favorable SOFC cathode properties and oxygen permeability arise from the outstanding ionic conductivities of BSFs. Wedig *et al.* evaluated the electrochemical activities of $A_{1-x}Sr_xCo_{1-y}Fe_yO_{3-\delta}$ (A = La, Ba, Bi) thin-film electrodes. They reported that the ionic conductivities of the Bi-based oxides are equal to or higher than these of the Ba-based MIECs [8]. This outstanding ionic conductivity can likely be attributed to the high polarizability of Bi^{3+}, which reduces the activation energy of oxide-ion diffusion [9]. Furthermore, Bi-based oxides have high durability with respect to CO_2 poisoning, one of the main problems of the Ba-based MIECs arising from the lower basicity of Bi^{3+} than that of Ba^{2+}. An example of this is $Bi_2Sr_2Nb_2MnO_{12-\delta}$, an oxide with a perovskite-related structure reported as an SOFC cathode material with a favorable CO_2 tolerance [10]. Another advantage of Co-free Bi-based oxides, or BSFs, is their low thermal expansion coefficient (TEC): the TECs of $Bi_{0.5}Sr_{0.5}FeO_{3-\delta}$ and $Bi_{0.7}Sr_{0.3}FeO_{3-\delta}$ are 12.4×10^{-6} [4] and 13.9×10^{-6} K^{-1} [11], respectively. These values are in the same range as those of SOFC electrolyte materials, such as Y-stabilized zirconia (YSZ).

Another characteristic of BSFs is that their surface exchange coefficient is not as high as that of the Ba-based MIECs [8]. One of the reasons for the low surface exchange kinetics of BSFs is the slow charge-transfer process of electronic carriers related to low electronic-hole conductivity [9]. In a recent study, the relationship between the surface exchange coefficients and hole conductivities was revealed for the $A_{1-x}Sr_xCo_{1-y}Fe_yO_{3-\delta}$ (A = Bi, Ba) system [8]. It is clear

*takamura@material.tohoku.ac.jp

 ©2019 American Physical Society

that deeper insight into the hole conduction properties of BSFs will be useful for improving their electrochemical activities.

Baek *et al.* were the first to report a discontinuous change in the electrical conductivity of $Bi_{0.7}Sr_{0.3}FeO_{3-\delta}$. A dramatic increase in the electrical conductivity measured in air was found during the heating process, with conductivity almost doubling at around 770 °C [11,12]. The results of the structural analysis they conducted using a high-temperature x-ray diffraction technique to determine the cause of the discontinuous change indicated no obvious change in the symmetry or in the lattice constants [12]. The mechanism of the discontinuous change of the hole conductivity remains unclear. The purpose of this study, therefore, is to clarify the origin of the discontinuous change of the hole conductivity of BSFs with their defect structure.

II. EXPERIMENTAL SECTION

$Bi_{1-x}Sr_xFeO_{3-\delta}$ ($x = 0.2$, 0.3, and 0.4), referred to as BSF20, 30, and 40, respectively, were synthesized by a solid-state reaction. Bi_2O_3, $SrCO_3$, and Fe_2O_3 were mixed in a stoichiometric molar ratio using a planetary ball mill in isopropanol. After evaporation, the pressed powders were calcined at 800–850 °C for 5 h in air. The calcined powders were again ground using a planetary ball mill for 24 h in isopropanol. Disks were formed by compaction using uniaxial pressing and further pressed at 200 MPa using a cold isostatic pressing apparatus. These disks were sintered at 970, 1000, or 1050 °C for BSF20, 30, and 40, respectively, for 5 h in air.

A crystal structure of the polished polycrystalline sample was investigated by XRD (Bruker AXS, AdvanceD8). Lattice constants were calculated by a whole-powder-pattern decomposition method. High-temperature x-ray diffractometry (HTXRD) was also performed to investigate the phase-transition behavior. The HTXRD was conducted during the cooling process from the highest temperature of 900 °C to eliminate the contribution of grain growth on the shape of the peak. Their microstructure was observed by SEM (JEOL, JSM-6360LA). The atomistic local structure of BSF30 was investigated by a C_s-corrected transmission electron microscope (JEOL, JEM-ARM200F) (TEM). Two samples were subjected to TEM analysis: the sample annealed at 725 °C for 16 h followed by slow cooling and the sample annealed at 900 °C for 1 h followed by quenching.

The electrical conductivity and the Seebeck coefficients were evaluated by a dc four-probe method using a precision power source (KEITHLEY, 2401 Source Meter) and a multimeter (KEITHLEY, 2401 MULTIMETER). Rectangular parallel-piped samples with dimensions of approximately $1.5 \times 2.7 \times 14$ mm^3 were cut from the polished disk. Pt paste was used as the electrode. Conductivity was measured in air or under a $P(O_2)$-controlled N_2-O_2 atmosphere. A convergence criterion of the conductivity measurement was 0.05% deviation during 10 min. After the convergence of conductivity, one side of the bar was locally heated with a microheater. The Seebeck coefficient was determined by the ratio of the thermoelectromotive force to the temperature difference measured between both sides. Three temperature gradients of approximately 10, 20, and 30 °C were used to calculate the Seebeck coefficient.

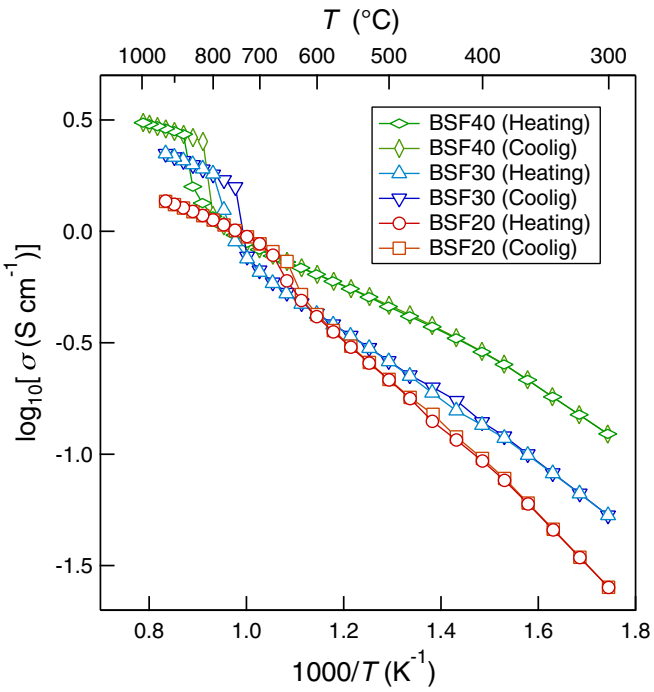

FIG. 1. Arrhenius-type plot of electrical conductivities of BSF20, 30, and 40 under air.

III. RESULTS AND DISCUSSION

A. Sample characterization

XRD patterns of sintered BSF20, 30, and 40 were assigned to a cubic perovskite-type structure (Fig. S1 in the Supplemental Material [13]). No other peak related to a secondary phase was observed in the XRD results. The calculated lattice constants of BSF20, 30, and 40 were 3.9552, 3.9509, and 3.9487 Å, respectively. The difference between these values and those reported by Li *et al.* is within 0.07–0.21%. The relative density was over 96%, which is favorable for evaluating electrical properties. The microstructure was observed by SEM (Fig. S2 [13]). Although the structure of BSF30 was almost homogeneous, in addition to pores, a small amount of a secondary phase ($Bi_2Fe_4O_9$-type phase) was observed. Wang *et al.* have also reported that a small amount of $Bi_2Fe_4O_9$ was formed in BSF30 fired at 850 °C [14]. The formation of the Fe-rich phase can be attributed to the volatility of Bi_2O_3. Meanwhile, because of the small amount of the secondary phase, its contribution to the electrical conduction properties was considered negligible.

B. Electrical conduction properties and defect equilibrium of BSF30 at high temperatures

Temperature dependencies of the total electrical conductivities of BSF20, 30, and 40 under air are plotted in Fig. 1. Because of the low ionic conductivity in air, as shown later, these conductivities can be regarded as hole conductivity [7]. The activation energy of the hole conduction of BSF30 was calculated by the following equation:

$$\sigma_p \propto \mu_p = \frac{A}{T} \exp\left(\frac{E_a}{k_B T}\right), \quad (1)$$

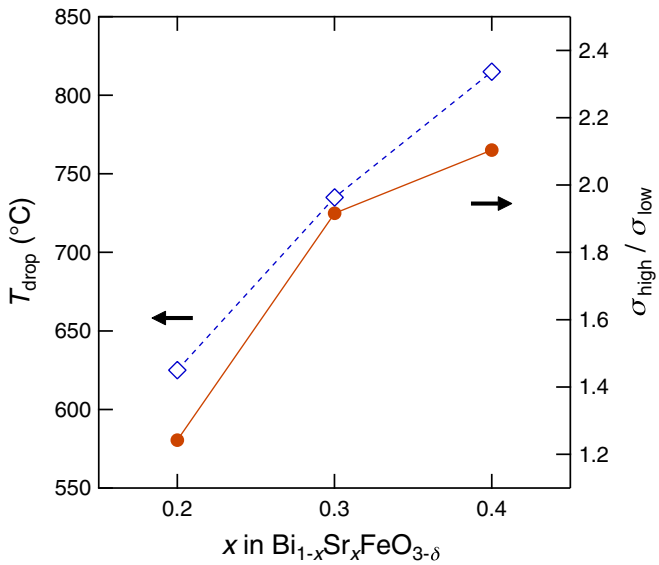

FIG. 2. Sr content dependence of the transition temperature, where conductivity drops in the cooling process (left axis) and the conductivity ratio of before and after the transition (right axis).

where μ_p, E_a, k_B, and A denote hole mobility, activation energy, the Boltzmann constant, and a constant, respectively. $\log_{10}(\sigma T)$ and T^{-1} showed a linear relationship (Fig. S3 [13]). The activation energies in the high- and low-temperature region were 0.36 and 0.30 eV, respectively. These values agree well with the activation energy of hole hopping conduction reported for 3d-transition-metal-based perovskite-type oxides [15–17].

Discontinuous conductivity changes at around 600–900 °C were confirmed not only in BSF30 but also in BSF20 and 40. Figure 2 shows the Sr content dependence of the transition temperature, where conductivity drops in the cooling process (left axis) and the conductivity ratio of before and after the transition (right axis). The transition temperature and the conductivity ratio showed a linear dependence with respect to Sr content. This implies that the transition originates from defects induced by Sr substitution. It should also be noted that the discontinuous change shows temperature hysteresis (Fig. 1). This suggests that the discontinuous change is a first-order phase transition.

In an attempt to find further evidence that the change in discontinuous conductivity is related to the first-order phase transition and involves the defects introduced, the temperature dependence of the total electrical conductivity of the BSF30 under air was evaluated in detail around the discontinuous change temperature. Figure 3 shows the temperature dependences of the electrical conductivity and dwelling time required to reach equilibrium at each temperature. It is interesting to note that dwelling time drastically increases around the hysteresis temperature region; it takes a maximum 10 h at 795 °C and 16 h at 735 °C for the heating and cooling process, respectively. This is evidence that the change in discontinuity is a lengthy process. Given that the phase transition occurs in a high-temperature region over 700 °C, the discontinuous change is presumably caused by a process involving ionic diffusion.

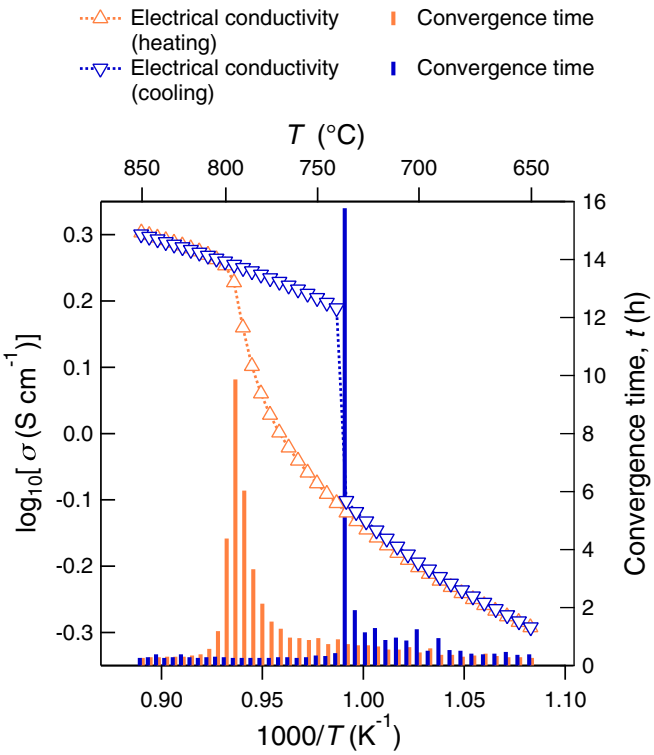

FIG. 3. Temperature dependences of the electrical conductivity and dwelling time required to reach equilibrium at each temperature.

To further clarify the nature of this phase transition, the $P(O_2)$ dependencies of both the total electrical conductivity and the Seebeck coefficient were measured. The results are shown in Figs. 4(a) and 4(b), respectively, with the Seebeck coefficient normalized as a dimensionless parameter. They clearly show a logarithmically linear dependence with a slope of $\pm 1/4$. The characteristics of the defect equilibrium of BSFs explain the $P(O_2)$ dependence. Given that the hole is considered to be $(Fe^{4+})^{\cdot}_{Fe^{3+}}$ in Fe-containing perovskite-type oxides [18], the redox reaction can be expressed as follows:

$$2(Fe^{4+})^{\cdot}_{Fe} + O^{\times}_{O} = 2(Fe^{3+})^{\times}_{Fe} + V^{\cdot\cdot}_{O} + \tfrac{1}{2}O_2. \quad (2)$$

Assuming that the equilibrium constant of this reaction is K_{red}, the hole concentration, that is to say, the concentration of Fe^{4+}, is expressed by the following equation:

$$p = [Fe^{4+}] = \frac{[Fe^{3+}]}{K_{red}}\left(\frac{[V^{\cdot\cdot}_{O}]}{[O^{\times}_{O}]}\right)^{\frac{1}{2}} P(O_2)^{\frac{1}{4}}. \quad (3)$$

Even though the Sr acceptors can be compensated by either the oxygen vacancies or holes, here it is assumed that the acceptor is fully compensated by the formation of an oxygen vacancy as follows:

$$[Sr'_{Bi}] \approx 2[V^{\cdot\cdot}_{O}] \approx \text{const.} \quad (4)$$

In this case, the hole concentration in Eqs. (3) should follow $+1/4$ dependence with respect to $\log_{10} P(O_2)$. Meanwhile, ionic conductivity is independent of $P(O_2)$ because the oxygen vacancy concentration is constant. As a result, total

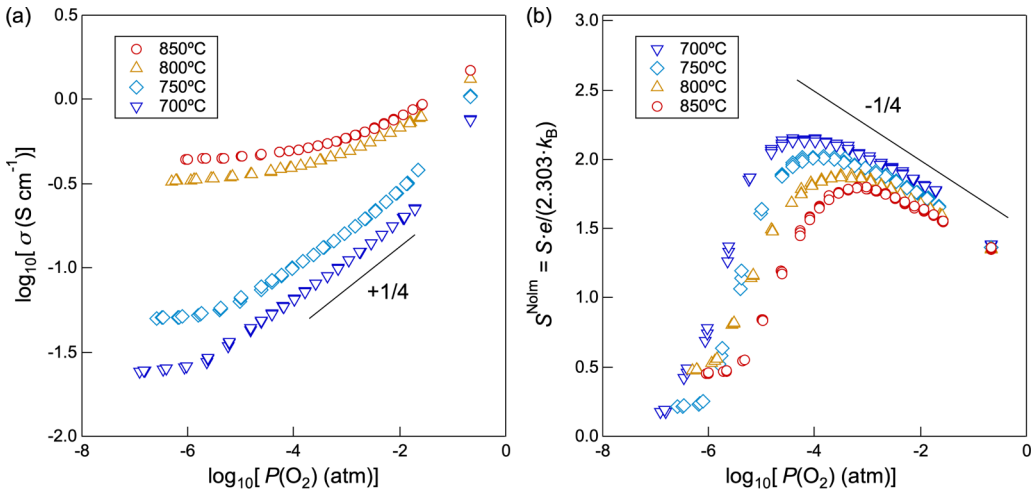

FIG. 4. $P(O_2)$ dependencies of both (a) the total electrical conductivity and (b) the normalized dimensionless Seebeck coefficient.

electrical conductivity can be expressed as follows:

$$\sigma = \sigma_p + \sigma_{ion} = AP(O_2)^{\frac{1}{4}} + \sigma_{ion} \approx \begin{cases} AP(O_2)^{\frac{1}{4}} & (\sigma_p \gg \sigma_{ion}), \\ \sigma_{ion} & (\sigma_p \ll \sigma_{ion}), \end{cases} \quad (5)$$

where A denotes a constant.

The Seebeck coefficient consists of contributions from electrons, holes, and ions. In BSF30 under a high $P(O_2)$ region [$P(O_2) > 10^{-3}$ atm], p-type conduction is dominant, as shown in Fig. 4(a). Thus, in this $P(O_2)$ region, the Seebeck coefficient can be regarded as the hole Seebeck coefficient, S_p. The following equation can be obtained by applying the theoretical formula of a Seebeck coefficient [18] to BSF30:

$$S \approx S_p \approx \frac{k_B}{e} \ln\left(\frac{1}{5/6}\frac{[Fe^{3+}]}{[Fe^{4+}]}\right), \quad (6)$$

where e and k_B denote the elementary charge and the Boltzmann constant, respectively. Substituting Eqs. (3) into this equation yields the following equation:

$$S \approx S_p \approx \frac{2.303k_B}{e}\left[\log_{10}\left(\frac{K_{red}}{5/6}\left(\frac{[V_O^{\cdot\cdot}]}{[O_O^{\times}]}\right)^{\frac{1}{2}}\right) - \frac{1}{4}\log_{10} P(O_2)\right]. \quad (7)$$

Assuming that most Sr acceptors are compensated by oxygen vacancies, the first term in the square brackets can be regarded as a constant. The following equation is then obtained:

$$S^{norm} \approx S_p^{norm} \stackrel{def}{=} \frac{S_p e}{2.303k_B} \approx -\frac{1}{4}\log_{10} P(O_2) + \text{const}, \quad (8)$$

where S^{norm} denotes a normalized dimensionless Seebeck coefficient. A slope of $-1/4$ with respect to $\log_{10} P(O_2)$ is then expected for the p-type conduction-dominated region. This dependence can be clearly observed in Fig. 4(b).

The origin of the phase transition can be understood in terms of these $P(O_2)$ dependencies of electrical conductivity and the Seebeck coefficient. The $P(O_2)$ dependence of the total electrical conductivity of BSF30 [Fig. 4(a)] shows a slope of $+1/4$ (σ_p) followed by a plateau regime (σ_{ion}) at all temperatures measured. This means that Eq. (4) holds for the whole $P(O_2)$ region [$10^{-7} < P(O_2) < 0.21$ atm] regardless of temperature.

Meanwhile, the hole and ionic conductivity of BSF30 discontinuously increased above its phase-transition temperature (around 790 °C) despite the slight but continuous decrease in the Seebeck coefficient. This indicates that the mobility but not the concentration of holes or oxide ions drastically changes at the phase-transition points because the electrical conductivity reflects both mobility and concentration while the Seebeck coefficient only reflects the concentration. As seen in Fig. 4(a), the ionic conductivity of BSF30 can be derived from the plateau regime [$10^{-7} < P(O_2) < 10^{-6}$ atm]. The ionic conductivity of the high-temperature phase (the phase above the transition temperature) and the low-temperature phase (the phase below the transition temperature) was 0.33 S cm^{-1} at 800 °C and 0.050 S cm^{-1} at 750 °C, respectively. The ionic conductivity of the high-temperature phase at 800 °C (0.33 S cm^{-1}) is approximately twice that of $La_{0.8}Sr_{0.2}Ga_{0.83}Mg_{0.17}O_{2.815}$, a favorable ionic conductor with a perovskite-type structure [19]. This value agrees with the reported values of 0.41 and 0.17 S cm^{-1} at 800 °C evaluated by electrical conductivity measurements under low oxygen partial pressure and an oxygen permeation test, respectively [11]. It should also be noted that the effect of phase transition on oxide-ion transport is much greater than on hole conduction. The ratio of conductivities at 800–750 °C for the ionic conductivity and the hole conductivity was 6.5 and 2.1, respectively. This implies that the phase transition is related to the ordering of oxygen vacancies.

C. Defect structure analysis of BSF30

The phase-transition behavior suggested by the discontinuous change of the electrical conductivity is then directly analyzed by HTXRD and TEM. The HTXRD patterns of BSF30 measured during the cooling process from 850 to 450 °C are displayed in Fig. 5(a). Given that the transition temperature of BSF30 is 735 °C (Fig. 3), the XRD patterns taken at 850–750 °C and 650–450 °C correspond to the high-

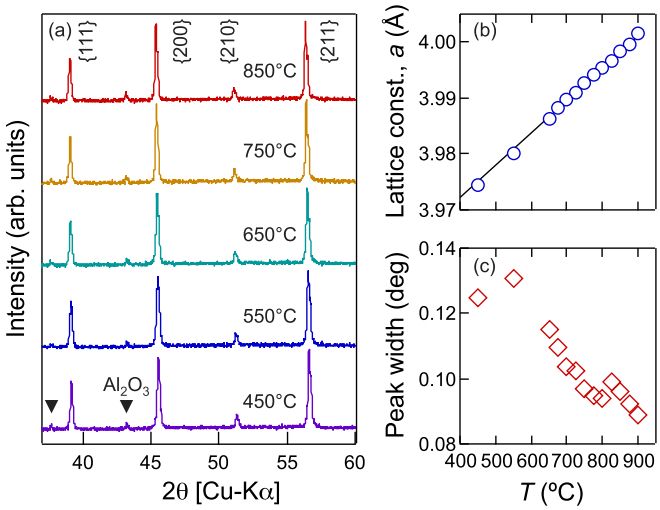

FIG. 5. (a) HTXRD patterns of BSF30 measured during the cooling process. Temperature dependences of (b) the lattice constant and (c) the peak width corresponding to the {200} planes.

and low-temperature phases, respectively. The absence of an obvious change in the XRD patterns is consistent with earlier findings [12]; all XRD patterns were fitted by a cubic perovskite-type structure regardless of the temperature. The peak attributed to Al_2O_3 is due to the sample holder. The temperature dependences of the lattice constant and peak width were calculated as shown in Figs. 5(b) and 5(c), respectively. The lattice constant [Fig. 5(b)] varied linearly over the whole temperature range, including the phase-transition region. Meanwhile, the peak width corresponding to the {200} planes [Fig. 5(c)] starts to increase at around the transition temperature and increases with decreasing temperature. This peak broadening suggests that the lattice is slightly distorted in the low-temperature phase. It can also be said that the phase transition causing a discontinuous change in the electrical conductivity is due to a small change in the crystal structure, but the change is not significant enough to result in a change in symmetry. To further investigate the structural transition, the time dependence of the peak width corresponding to the {200} planes was evaluated. BSF30 was first annealed at 900 °C for 20 h, and then kept at 725 °C, a temperature slightly lower than the phase-transition temperature. As shown in Fig. S4 [13], the peak width slowly increased as time elapsed. It took approximately 15 h to reach equilibrium; this time scale is comparable to the electrical conductivity relaxation shown in Fig. 3. This is further evidence that the change in electrical conductivity is correlated to the oxygen vacancy ordering.

The local crystal structure of BSF30 was observed using HRTEM and STEM with atomistic resolution to investigate the slight change in the crystal structure. A TEM sample for the low-temperature phase was prepared by annealing at 725 °C, which is just below the phase-transition temperature, for 16 h in air followed by slow cooling. A TEM sample of the high-temperature phase was prepared by quenching after annealing at 900 °C, which is more than 100 °C higher than the transition temperature, for 1 h in air. To confirm that the high-temperature phase was fully quenched, the electrical conductivity of the quenched sample was measured (Fig. S5 [13]). Its electrical conductivity was higher than that of the low-temperature phase by a factor of approximately 2.5 at 300 °C. Meanwhile, the higher conductivity gradually decreased with increasing temperature, especially at around 450 and 650 °C. This behavior is evidence that the high-temperature phase was fully quenched.

An HRTEM image of the low-temperature phase of BSF30 taken from a $[1\bar{1}0]$ incident beam direction is shown in Fig. 6(a). Stripe contrasts can be observed especially in the lower part of the image. The diffraction pattern of the whole area is shown in Fig. 6(b). Diffraction spots attributed to long-range ordering emerged in addition to the basic diffraction pattern of the cubic perovskite-type structure. These additional spots were found to have fivefold d-spacing of {001}, as shown in Fig. 6(c). In addition to the fivefold period, evidence of a twofold period can be seen in both the {001} and {110} directions. Such long-range ordering was also reported in $Bi_{0.75}Sr_{0.25}FeO_{3-\delta}$ (BSF25) [20] and $Bi_{0.55}Sr_{0.45}FeO_{3-\delta}$ (BSF55) [21]. It should also be noted that long-range ordering can be observed in limited areas but not over the whole area shown in Fig. 6(a). In fact, an FFT image taken from the orange (dashed line) box region [Figs. 6(e) and 6(f)] shows the fivefold period; no such spots can be seen in the FFT image taken from the blue box (chain line) region [Figs. 6(g) and 6(h)]. This coexistence of domains was also reported in BSF55 [21].

To further clarify the nature of the long-range ordering, a STEM-HAADF image of the low-temperature phase of BSF30 was taken from the $[1\bar{1}0]$ incident beam direction, which is the same direction as the HRTEM image [Fig. 6(a)] shown in Fig. 7(a). The corresponding FFT image (inset) shows only the basic diffraction spots. It should be noted that an HAADF image basically reflects information related to the heavy elements, i.e., the cations, and the long-range ordering is not due to cation ordering, such as Bi and Sr. The long-range ordering with the fivefold d-spacing {001} in the STEM-ABF image [Fig. 7(b)] was taken from exactly the same region as the HAADF image. The fivefold periodicity can be clearly observed in the FFT image (inset). Unlike the HAAFDF image, light and heavy elements simultaneously contribute to an ABF image. Oxygen positions can be identified in the enlarged ABF image shown in Fig. 7(c). Based on these observations, it appears that the long-range ordering is due to anion ordering, presumably that of oxygen vacancies. The existence of an oxygen-deficient plane in BSF25 has been suggested based on the results of STEM-ABF observation in earlier research [20]: a remarkable position shift of oxide ions in the vicinity of the oxygen-deficient plane toward the plane was found. This shift was reported to result in a relaxation in the local environment of FeO_6 polyhedra. Even though the shift of the oxide ion is not clear in Fig. 7(b), the same behavior was expected in the low-temperature phase of BSF30. In the high-temperature phase of BSF30, however, a homogeneous structure without stripe contrasts was observed in the HRTEM image shown in Fig. S6 [13]. There were no additional spots in the diffraction pattern. Structural homogeneity was also confirmed by the STEM-HAADF and -ABF images [Figs. 8(a) and 8(b)] and the corresponding FFT images (inset). Therefore, no long-range ordering was formed in the high-temperature phase. This means that the phase transition of BSF30 which causes

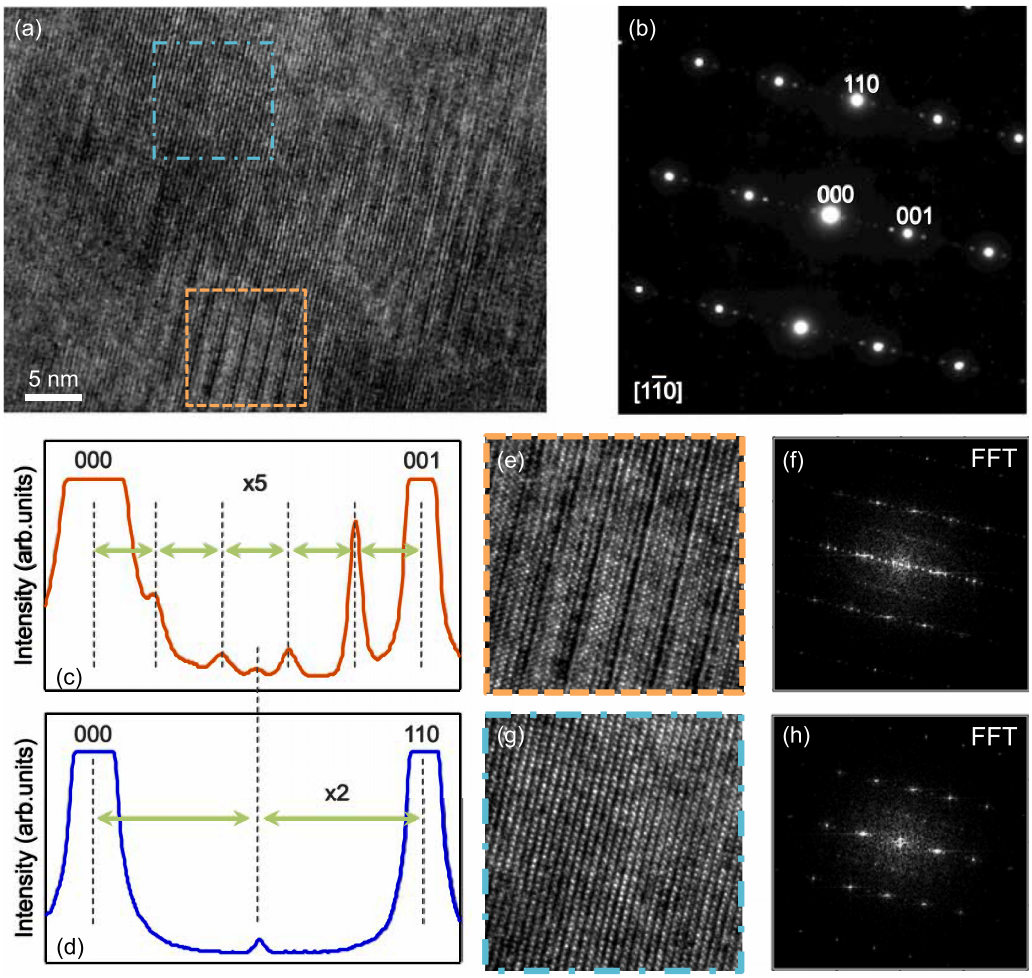

FIG. 6. (a) HRTEM image of the low-temperature phase of BSF30 taken from the [1$\bar{1}$0] incident beam direction. (b) Electron diffraction pattern corresponding to the whole area of (a). (c),(d) Line profiles of (b) along the 001 and 110 direction, respectively. (e),(g) Magnified images of a selected area in (a). (f),(h) Fast Fourier transform (FFT) images corresponding to (e) and (g), respectively.

the electrical conductivity change at around 770 °C is due to the order-disorder phenomenon of anions (oxygen vacancies). To confirm that the stripe contrast observed in the HRTEM image [Fig. 6(a)] arises from oxygen vacancy ordering, HRTEM images of the high- and low-temperature phases of BSF30 taken from the [1$\bar{1}$0] incident beam direction were simulated by QSTEM software. An ideal cubic perovskite-type structure and a $1 \times 1 \times 5$ superstructure with one oxygen-deficient

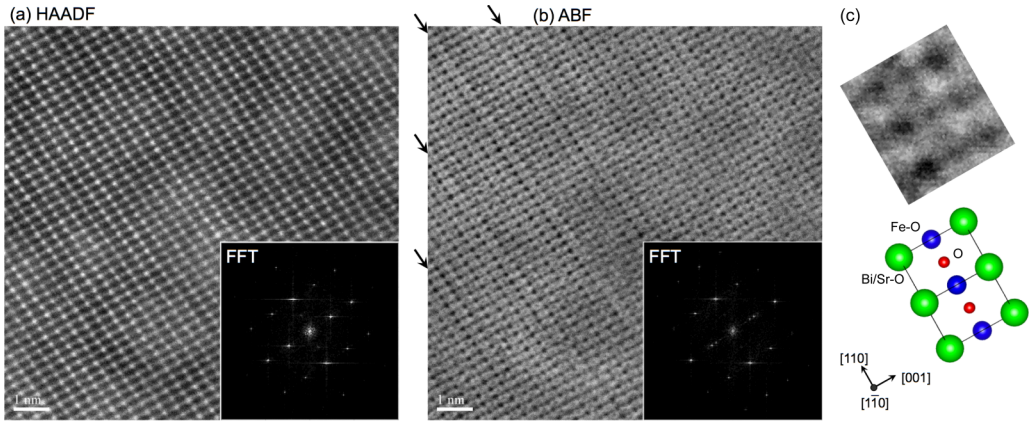

FIG. 7. (a) STEM-HAADF and (b) -ABF images of the low-temperature phase of BSF30 taken from the [1$\bar{1}$0] incident beam direction. The insets are the corresponding FFT images. The arrows in (b) indicate the long-range ordering. (c) A magnified STEM-ABF image and the corresponding schematic crystal structure.

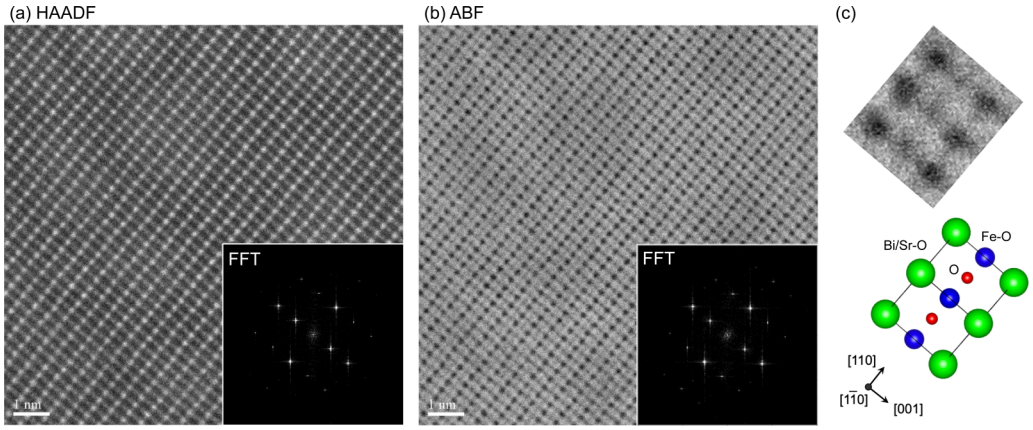

FIG. 8. (a) STEM-HAADF and (b) -ABF images of the high-temperature phase of BSF30 taken from the [1$\bar{1}$0] incident beam direction. The insets are the corresponding FFT images. (c) A magnified STEM-ABF image and the corresponding schematic crystal structure.

layer parallel to the {001} plane were used for the simulation of the high- and low-temperature phases, respectively. As shown in Fig. S7 [13], dark stripes with an interval of fivefold d-spacing of {001} were observed in the simulated image of the low-temperature phase, but not in that of the high-temperature phase. These simulated images show good agreement with the experimental images.

The role of the order-disorder transition of oxygen vacancies in both the hole and ionic conductivity of BSFs can be determined based on the results above. Based on the theory of double hopping conduction [22], a hole localized on an Fe ion moves to the next Fe ion via the oxide ion sandwiched by them. Because oxygen-deficient planes formed in the low-temperature phase, the holes scatter, reducing mobility in both holes. Hole conductivity is, therefore, also reduced. This explanation agrees well with the fact that the discontinuous change in the hole conductivity is caused not by a change in the concentration but by the hole mobility [Fig. 4(b)]. Given that most Sr acceptors are compensated by oxygen vacancies in BSFs, the region with an ordered domain should become larger with increasing Sr content. More Sr substitution, therefore, results in a larger drop in the hole mobility at the transition to the low-temperature phase. This seems to be the reason for the positive correlation between Sr content and the conductivity ratio both before and after the transition (Fig. 2). Moreover, the trapped state of oxygen vacancies forming the oxygen-deficient planes results in lower oxide-ion mobility. This segregation of oxygen vacancies also explains the ionic conductivity drop at the transition to the low-temperature phase [Fig. 4(a)].

The long-range ordered structure in BSFs can be determined based on the acceptor content. The order-disorder structure has not only been observed in BSFs, but it has also been reported in Ca-doped samples, $Bi_{1-x}Ca_xFeO_{3-\delta}$ [23,24]. As shown in Fig. 9, the period of the ordered structure is inversely proportional to the acceptor content. Assuming an oxygen-deficient plane is inserted at n-fold d-spacing of {001}, the chemical composition of the perovskite-type oxide can be expressed as $ABO_{(3n-1)/n}\square_{1/n}$ ($\square$ denotes oxygen vacancy). The oxygen vacancy concentration of this compound is then given by $1/(3n)$ as a site proportion to the entire O site. Meanwhile, given that most acceptors (A') are compensated by oxygen vacancies, the oxygen vacancy concentration of $A_{1-x}A'_xBO_{3-x/2}\square_{x/2}$ is given by $x/6$. These formulas drive the relation of $n = 2/x$, which explains the inverse relationship between periodicity (n) and the acceptor content (x). However, the actual periodicity is smaller than the value derived from this theoretical formula. For example, in the case of BSF30, the period derived from the theoretical formula is 6.67, whereas the actually observed period is 5. This difference can be attributed to the segregation of oxygen vacancies in the ordered domain. In fact, a nominal concentration of oxygen vacancies in BSF30 is 5% while the oxygen vacancy concentration in the ordered domain with oxygen-deficient planes inserted in fivefold d-spacing of {001} is 6.7%. This suggests that it takes a long time for the oxygen vacancies to

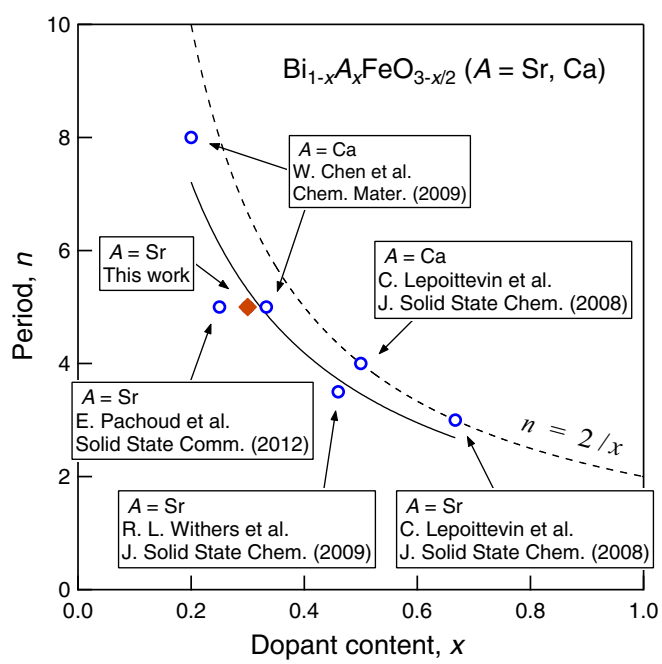

FIG. 9. Period of the long-range ordered structure as a function of dopant content of $Bi_{1-x}A_xFeO_{3-x/2}$ (A = Sr,Ca). The solid and dashed curves indicate the fitting of the experimental data [20,21,23,24] and the theoretical relationship, respectively.

fully order and to form fully the uniform defect-layer spacing. This also explains the slow oxygen vacancy order-disorder transition observed in Fig. 3.

These results suggest that it is possible to control and manage the ordering phenomena with respect to the specific requirements for certain applications of BSFs. The stabilization of the high-temperature (disordered) phase is effective to improve the electrochemical activity of BSFs in the intermediate temperature range. Even though the hole conductivity of BSFs is enhanced by doping with more Sr, the transition temperature also rises. In other words, a dilemma occurs in the Bi-Sr-Fe ternary system. It is therefore necessary to adopt other techniques such as a substitution of another element. Since the coordination number of the B site in the vicinity of the oxygen-deficient planes becomes less than that in the ideal structure, the high-temperature phase may be stabilized by replacing the B site with an element with a larger ionic radius and which favors sixfold coordination, such as Sc^{3+} or Y^{3+}. Furthermore, the order-disorder transition of BSFs is also attractive from the perspective of potential multiferroic applications. According to Scott and Dawber, oxygen vacancy ordering causes fatigue in perovskite-type ferroelectrics; moreover, the crystallographic direction of domain-wall pinning is affected by the direction of the oxygen-deficient planes [25]. Noguchi *et al.* demonstrated that the accumulation of oxygen vacancies at the interface between a ferroelectric oxide and an electrode, which is the main reason for the diminished switching capacity, can be suppressed by dopants trapping oxygen vacancies [26]. As mentioned above, oxygen vacancy ordering lowers the diffusivity of the oxygen vacancy in BSF30. It is therefore reasonable to assume that switching capacity is improved by utilizing the ordering behavior. If the order-disorder structure for epitaxial thin films of BSFs can be controlled, their polarization behavior, which can be affected by the oxygen-deficient planes, can be managed. Although it is a case of a double perovskite-type oxide, it has been reported that such magnetic properties as spontaneous magnetization also change drastically with a degree of oxygen vacancy ordering, and this can be altered by controlling the cooling rate of annealing conditions [27]. Thermal history is a key factor in determining the multiferroic properties of BSFs even at room temperature. Controlling the ordering behavior can also have the effect of improving the properties of Bi-Fe-based perovskite-type oxides as random access memory (ReRAM) [28]; in fact, Park *et al.* reported that an ordered oxygen vacancy chain works as a nucleus site of a conductive filament in TiO_2 [29].

IV. CONCLUSION

The electrical conduction properties, the defect equilibrium, and the local defect structure of BSF20, 30, and 40 with a perovskite-type structure were investigated with a focus on the discontinuous change in electrical conductivity at high temperatures. All the samples showed a change in discontinuous conductivity with respect to temperature in the temperature range of 600–800 °C. The magnitude of the discontinuous change was shown to depend on the Sr content; a higher Sr content has a higher transition temperature and magnitude. In BSF30, most Sr acceptors were compensated by oxygen vacancies, and this defect equilibrium was shown to be the same for the whole temperature region. The temperature and $P(O_2)$ dependences of electrical conductivity reveal that it is the change in mobility but not in the concentration term of charge carriers that causes the discontinuous change in both the hole and oxide-ion conductivities. This discontinuous change is caused by an order-disorder transition of oxygen vacancies. In the low-temperature ordered phase of BSF30, domains emerge with oxygen-deficient planes characterized by fivefold d-spacing of {001}. The periodicity of the oxygen-deficient planes is inversely proportional to the acceptor content. Meanwhile, the oxygen-deficient planes disappear in the high-temperature disordered phase. The results of this study show that it is possible to control the order-disorder transition of BSFs, which strongly affects their electrical conduction properties, to attain the specific characteristics required for various electrochemical and multiferroic applications.

ACKNOWLEDGMENTS

This work has been financially supported in part by JSPS KAKENHI Grant No. 18H03832. Y.T. would like to express his appreciation for the financial support from the Interdepartmental Doctoral Degree Program for Multi-dimensional Materials Science Leaders in Tohoku University.

[1] G. Catalan and J. F. Scott, Physics and applications of bismuth ferrite, Adv. Mater. **21**, 2463 (2009).

[2] T. Hussain, S. A. Siddiqi, S. Atiq, and M. S. Awan, Induced modifications in the properties of Sr doped $BiFeO_3$ multiferroics, Prog. Nat. Sci.: Mater. Int. **23**, 487 (2013).

[3] K. Brinkman, T. Iijima, and H. Takamura, Acceptor doped $BiFeO_3$ ceramics: A new material for oxygen permeation membranes, Jpn. J. Appl. Phys. **46**, L93 (2007).

[4] Y. Niu, W. Zhou, J. Sunarso, L. Ge, Z. Zhu, and Z. Shao, High performance cobalt-free perovskite cathode for intermediate temperature solid oxide fuel cells, J. Mater. Chem. **20**, 9619 (2010).

[5] D. S. Khaerudini, G. Guan, P. Zhang, X. Hao, Z. Wang, C. Xue, Y. Kasai, and A. Abudula, Performance assessment of $Bi_{0.3}Sr_{0.7}Co_{0.3}Fe_{0.7}O_{3-\delta}$-LSCF composite as cathode for intermediate-temperature solid oxide fuel cells with $La_{0.8}Sr_{0.2}Ga_{0.8}Mg_{0.2}O_{3-\delta}$ electrolyte, J. Power Sources **298**, 269 (2015).

[6] D. S. Khaerudini, G. Guan, P. Zhang, X. Hao, Z. Wang, Y. Kasai, K. Sasagawa, and A. Abudula, Evaluation of $(Bi_{0.4}Sr_{0.6})_xCo_{0.3}Fe_{0.7}O_{3-\delta}$ ($x = 0.7, 0.8, 0.9, 1.0, 1.1$) perovskite-type oxide as potential cathode for intermediate-temperature solid oxide fuel cells, Int. J. Hydrogen Energy **40**, 11011 (2015).

[7] K. Brinkman, T. Iijima, and H. Takamura, The oxygen permeation characteristics of $Bi_{1-x}Sr_xFeO_3$ mixed ionic and electronic conducting ceramics, Solid State Ion. **181**, 53 (2010).

[8] A. Wedig, R. Merkle, and J. Maier, Oxygen exchange kinetics of $(Bi,Sr)(Co,Fe)O_{3-\delta}$ thin-film microelectrodes, J. Electrochem. Soc. **161**, F23 (2014).

[9] Y. Niu, J. Sunarso, F. Liang, W. Zhou, Z. Zhu, and Z. Shao, A comparative study of oxygen reduction reaction on Bi- and La-doped $SrFeO_{3-\delta}$ perovskite cathodes, J. Electrochem. Soc. **158**, B132 (2011).

[10] Y. Zhu, W. Zhou, Y. Chen, and Z. Shao, An aurivillius oxide based cathode with excellent CO_2 tolerance for intermediate-temperature solid oxide fuel cells, Angew. Chem., Int. Ed. **55**, 8988 (2016).

[11] D. Baek, A. Kamegawa, and H. Takamura, Mixed conductivity and electrode properties of Mn-doped Bi-Sr-Fe-based perovskite-type oxides, Solid State Ion. **253**, 211 (2013).

[12] D. Baek and H. Takamura, Preparation and mixed conductivity of Mn-doped Bi-Sr-Fe-based perovskite type oxides, in *Proceedings of the 13th Asian Conference on Solid State Ionics 192* (Sendai, 2012).

[13] See Supplemental Material http://link.aps.org/supplemental/10.1103/PhysRevMaterials.3.125802 for further information of XRD patterns, a SEM image, electrical conductivities, and a HRTEM image.

[14] L. Y. Wang, D. H. Wang, H. B. Huang, Z. D. Han, Q. Q. Cao, B. X. Gu, and Y. W. Du, The magnetic properties of polycrystalline $Bi_{1-x}Sr_xFeO_3$ ceramics, J. Alloys Compd. **469**, 1 (2009).

[15] D. Salazar, D. Arias, O. J. Durá, and M. A. López De La Torre, Thermopower and electrical resistivity of $La_{1-x}Sr_xMnO_3$ (x = 0.2,0.3): Effect of nanostructure on small polaron transport, J. Alloys Compd. **583**, 141 (2014).

[16] W. H. Jung, Transport mechanisms in $La_{0.7}Sr_{0.3}FeO_3$: Evidence for small polaron formation, Physica B **299**, 120 (2001).

[17] K. K. Bhargav, S. Ram, and S. B. Majumder, Small polaron conduction in lead modified lanthanum ferrite ceramics, J. Alloys Compd. **638**, 334 (2015).

[18] J.-I. Jung, S. T. Misture, and D. D. Edwards, Seebeck coefficient and electrical conductivity of BSCF ($Ba_{0.5}Sr_{0.5}Co_xFe_{1-x}O_{3-\delta}$, $0 \leqslant x \leqslant 0.8$) as a function of temperature and partial oxygen pressure, Solid State Ion. **206**, 50 (2012).

[19] K. Huang, R. S. Tichy, and J. B. Goodenough, Superior perovskite oxide-ion conductor; strontium- and magnesium-doped $LaGaO_3$: I, phase relationships and electrical properties, J. Am. Ceram. Soc. **81**, 2565 (1998).

[20] E. Pachoud, Y. Bréard, C. Martin, A. Maignan, A. M. Abakumov, E. Suard, R. I. Smith, and M. R. Suchomel, $Bi_{0.75}Sr_{0.25}FeO_{3-\delta}$: Revealing order/disorder phenomena by combining diffraction techniques, Solid State Commun. **152**, 331 (2012).

[21] R. L. Withers, L. Bourgeois, K. Balamurugan, N. H. Kumar, P. N. Santhosh, and P. M. Woodward, A TEM investigation of the $(Bi_{1-x}Sr_x)Fe^{3+}O_{3-x/2}$, $0.2 \leqslant x \leqslant 0.67$, solid solution and a suggested superspace structural description thereof, J. Solid State Chem. **182**, 2176 (2009).

[22] C. Zener, Interaction between the d-shells in the transition metals. II. Ferromagnetic compounds of manganese with perovskite structure, Phys. Rev. **82**, 403 (1951).

[23] C. Lepoittevin, S. Malo, N. Barrier, N. Nguyen, G. Van Tendeloo, and M. Hervieu, Long-range ordering in the $Bi_{1-x}Ae_xFeO_{3-x/2}$ perovskites: $Bi_{1/3}Sr_{2/3}FeO_{2.67}$ and $Bi_{1/2}Ca_{1/2}FeO_{2.75}$, J. Solid State Chem. **181**, 2601 (2008).

[24] W.-T. Chen, A. J. Williams, L. Ortega-San-Martin, M. Li, D. C. Sinclair, W. Zhou, and J. P. Attfield, Robust antiferromagnetism and structural disorder in $Bi_xCa_{1-x}FeO_3$ perovskites, Chem. Mater. **21**, 2085 (2009).

[25] J. F. Scott and M. Dawber, Oxygen-vacancy ordering as a fatigue mechanism in perovskite ferroelectrics, Appl. Phys. Lett. **76**, 3801 (2000).

[26] Y. Noguchi, H. Matsuo, Y. Kitanaka, and M. Miyayama, Ferroelectrics with a controlled oxygen-vacancy distribution by design, Sci. Rep. **9**, 4225 (2019).

[27] N. V. Kasper, I. O. Troyanchuk, D. D. Khalyavin, N. Hamad, L. Haupt, P. Fröbel, K. Bärner, E. Gmelin, Q. Huang, and J. W. Lynn, Effect of oxygen content and oxygen vacancy ordering on the properties of $TbBaCo_2O_{6-\delta}$ perovskites, Phys. Status Solidi B **215**, 697 (1999).

[28] A. Tsurumaki-Fukuchi, H. Yamada, and A. Sawa, *Resistive Switching Memory Based on Ferroelectric Polarization Reversal at Schottky-like* $BiFeO_3$ *Interfaces*, Materials Research Society Symposium Proceedings No. 1430 (MRS, Pittsburgh, 2012).

[29] S. Park, B. Magyari-Kope, and Y. Nishi, Impact of oxygen vacancy ordering on the formation of a conductive filament in TiO_2 for resistive switching memory, IEEE Electron Device Lett. **32**, 197 (2011).